APPLICATIONS OF PERCOLATION THEORY TO THE ANALYSIS OF COAL GASIFICATION

Sebastián Reyes and Klavs F. Jensen

Department of Chemical Engineering and Materials Science
University of Minnesota, Minneapolis, MN 55455

INTRODUCTION

The changes in pore structure, internal surface area, and transport characteristics of porous carbonaceous materials play a major role in their gasification behavior. To describe the complex interactions of physical and transport properties during char gasification, it is essential to have a realistic model for the evolution of geometrical and topological features of the pore space. Several models for the structural changes during gas-solid reactions have been developed (1-11) resulting in important contributions to the understanding of char gasification reactions. Nevertheless, refinements are needed since available models can successfully predict only a subset of experimental observations. Even though available structural models include key features of pore branching, important topological effects are lost when the influence of closed porosity is not taken into account and effective diffusion coefficients are evaluated through tortuosity factors. Another key topologically dependent property is the eventual fragmentation of the particle at a critical porosity. The uniform development of porosity in the kinetic regime causes particle disintegration preferentially at high conversions. On the other hand, when diffusional resistances are important, the critical porosity of fragmentation is reached first at the particle surface, causing the continuous shrinkage of the particle from the early stages of conversion. Consequently, the overall conversion is not only determined by the conversion level of the shrinking particle but also by the history of released fragments. An interesting treatment of particle shrinkage during char particle combustion has been presented by Gavalas (9). However, more detailed analysis is required to relate the critical porosity of fragmentation to the topology of the internal structure.

The objective of this paper is to present an application of percolation theory to the analysis of coal gasification. It is well known that inorganic impurities naturally present in char particles can catalyze gasification reactions (12). However, our primary objective is to improve the structural models. Realistic extensions may then be made to include catalytic effects. The present particle description focuses on structural and topological features not included in previous models. The use of percolation theory provides a natural framework for understanding and evaluating the role of pore opening, pore enlargement and pore overlap in the evolution of porosity and internal surface area. Moreover, it accurately describes the fundamental influence of pore topology on transport characteristics of the internal structure, as well as particle fragmentation phenomena at high porosities.

PERCOLATION CONCEPTS AND STRUCTURAL PROPERTIES

A general description of char gasification requires a model relating physical and transport properties to local structural changes. This model should accurately describe the accessible porosity (ϕ^A), accessible internal surface area per unit volume ($\hat{a}^A$), and effective transport coefficients (ε^E) as functions of local carbon conversion. The potential contributions from closed pores to the total surface area ($\hat{a}$) and total porosity (ϕ) can be locally described through the relations:

$$\phi^A = \phi - \phi^I \qquad 1)$$

$$\hat{a}^A = \hat{a} - \hat{a}^I \qquad 2)$$

where the superscript I on ϕ and $\hat{a}$ identify the isolated porosity and surface area. Equations 1 and 2 are necessary to account for pore opening by chemical reactions of the internal structure.

The effective transport coefficients are strongly dependent on the development of ϕ^A as well as on the size and geometry of the pores. That is, ϕ^A reflects the main topological features of the internal structure, such as dead ends and tortuous paths, which determine the extent of mass transport through the pore space. Moreover, if Knudsen diffusion is significant, the evolution of the pore size distribution also becomes a key factor in predicting transport.

Since a complete characterization of pore space morphology cannot be obtained by regular geometrical and topological simplifications, it is desirable to resort to some statistical description. This is supported by the observation that the majority of porous solids exhibit highly disordered structures. Consequently, the statistical means of percolation theory are ideally suited for evaluating ϕ^A, $\hat{a}^A$ and ϵ^E in terms of ϕ. Percolation theory, first introduced by Broadbent and Hammersley (13), has been successfully applied to describe numerous physical and mechanical phenomena in disordered media. Key concepts and details of the theory can be found in available review papers (e.g. (14-16)).

Transport and reactions in porous solids can be modelled, in principle, by constructing large space filling random structures. However, the computational effort involved surpasses available resources even in large scale computing facilities. Fortunately, key features of these models are captured by simple networks. Reyes and Jensen (17) have recently demonstrated that a network model of pore topology, a so-called Bethe network may be used to evaluate ϕ^A and ϵ^E in porous solids. A Bethe network is an endlessly branching tree lacking reconnections and completely characterized by its coordination number z. The coordination number is the number of bonds connecting each site. If a fraction ϕ of randomly selected bonds are labeled as "pores", ϕ^A is a unique function of ϕ and z. If ϕ is less than a nonzero threshold value ϕ_c, called the percolation threshold, the pore space consists of disconnected regions, i.e. isolated pores. The threshold value for Bethe networks is given by (18):

$$\phi_c = 1/(z-1) \qquad 3)$$

The network thus defined can be conveniently used to simulate topological features in porous solids. Since its topological properties are preserved by increasing or decreasing the length and/or the cross-section of the bonds, the experimentally measured porosity, ϕ^A, and pore size distribution, f(r), can be readily matched to the network model by randomly removing a fraction $1-\phi(\phi^A,z)$ of bonds and distributing sizes to a fraction $\phi(\phi^A,z)$ according to f(r). To completely specify the appropriate network model simulating the pore space of the porous solid, the coordination number of the Bethe network must be selected. This number is chosen to match the percolation threshold of the Bethe network and the porous solid. ϕ_c for the solid can be determined from fragmentation studies (19) through the relation:

$$\phi_c = 1 - \phi^* \qquad 4)$$

where ϕ^* is the critical porosity of fragmentation. An alternative approach is to directly determine z from experimental data on effective diffusion coefficients (17). A schematic representation of accessible pore space simulated by a 3-coordinated Bethe network is shown in Figure 1 for arbitrary inputs of ϕ^A and f(r). The attractiveness of this approach is that effective transport coefficients can be exactly evaluated for binary mixtures without resorting to tortuosity factors while explicitly accounting for the influences of narrow necks, tortuous paths and dead ends. Close agreement has been found between predictions with this method and published experimental data on effective diffusion coefficients (17). As an example, Table 1 shows experimentally measured diffusion coefficients for the pair CO-CO_2 in porous

electrode graphite (20), and predicted values with a 5-coordinated Bethe network. Predicted values are in excellent agreement with measurements for a wide range of temperatures (18-900°C) and pressures (0.1-10 atm). Moreover, this approach allows a natural extension for evaluating ε^E in changing structures, since input values of ϕ and f(r), characterizing the local morphology, can be determined from independent balance equations.

By using the present Bethe network representation of the pore space, particle fragmentation may be modelled by Equations 3 and 4. Once the appropriate coordination number has been selected, both ϕ_c and ϕ^* are determined. However, it should be emphasized that ϕ^* is based solely on topological features of two-phase structures leading to particle breakup by reactions, and not to mechanical phenomena, such as abrasion. The mass distribution of released fragments may be estimated as (21):

$$g(r,z) = \frac{z[(z-1)n]!}{(n-1)![(z-2)n+2]!} \cdot \frac{(z-2)^{(z-2)n+2}}{(z-1)^{(z-1)n+2}} \qquad 5)$$

where n is an integer number representing the size of the cluster whose mass is nm_f, with m_f being the mass of the smallest fractal unit characterizing the structure.

To complete the framework for a gasification model, the accessible internal surface area must be related to the local structure. Consistent with the Bethe network formulation, and based on probabilistic arguments, $\hat{a}^A$ can be estimated as (21):

$$\hat{a}^A = K\{\phi(1-\phi) - \phi^I(\phi,z)[1 - \phi^I(\phi,z)]\} \qquad 6)$$

The constant K is related to the mass per unit volume of a fractal unit, and can be obtained by matching $\hat{a}^A$ to a single surface area determination. The important implications of this approach are that effects of pore enlargement and pore overlap become natural consequences of increasing ϕ in a random fashion.

GASIFICATION MODEL

Gasification of a single char particle in CO_2 is chosen to illustrate the percolation based approach outlined in the previous section. It is further assumed that there are no catalytically active mineral impurities in the char. The evaluation of physical, transport and fragmentation properties require initial data readily available by conventional characterization of porous solids (e.g. ϕ_o^A, $\hat{a}_o^A$, $f_o(r)$), except for the coordination number of the network. This number can be implied from experimental data on diffusion coefficients or fragmentation studies. However, here it is considered as a parameter to simulate gasification behavior of char particles with varoius levels of pore space connectivity. Typical values fall in the range 4 to 8 (17).

The reaction is considered to be first order in CO_2. Since this reaction leads to an increase in the number of moles, mass transfer contributions from both concentration and pressure gradients must be included in the model equations. The derivation of the appropriate equations describing the gasification behavior for the above conditions has been presented elsewhere (22). In dimensionless form, modelling equations may be summarized as:

Mass balances for gaseous components: $i \neq j = CO, CO_2$

$$0 = \frac{1}{\eta^2}\frac{1}{\xi^2}\frac{\partial}{\partial\xi}\left[\xi^2\varepsilon_{ij}^{ED}\lambda\frac{\partial X_i}{\partial\xi} + \xi^2\varepsilon_{ij}^{EP}X_i\frac{\partial\lambda}{\partial\xi}\right] + \nu_i\psi_o^2 S\lambda X_{CO_2} \qquad 7)$$

$$X_i(\xi,0) = 0 \qquad 8)$$

$$\partial X_i(0,\tau)/\partial\xi = 0 \qquad 9)$$

$$\left\{\varepsilon^{ED}_{ij}\lambda \frac{\partial X_i}{\partial \xi} + \varepsilon^{EP}_{ij} X_i \frac{\partial \lambda}{\partial \xi}\right\}\Bigg|_{\xi=1} = \eta\, B_{mi}\left(X_{ib} - X_i(1,\tau)\right) \qquad 10)$$

Mass balance for solid phase:

$$\frac{d\phi}{d\tau} = \sigma_o S \lambda X_{CO_2} + \frac{\xi}{\eta}\frac{\partial \phi}{\partial \xi}\frac{d\eta}{d\tau} \qquad 11)$$

$$\gamma(\xi,0) = \phi_o \qquad 12)$$

Rate of particle shrinkage:

$$\frac{d\eta}{d\tau} = -\left\{\lambda X_{CO_2}\right\}\Big|_{\xi=1} \qquad \tau \leq \tau^* \qquad 13)$$

$$\eta(0) = 1$$

$$\frac{d\eta}{d\tau} = -\eta\left\{\frac{\sigma_o S \lambda X_{CO_2}}{\partial\phi/\partial\xi}\right\}\Bigg|_{\xi=1} \qquad \tau > \tau^* \qquad 14)$$

$$\eta(\tau^*_+) = \eta(\tau^*_-)$$

Pore growth:

$$\zeta(\xi,\tau) = F(\xi,\tau)/S(\xi,\tau) \qquad 15)$$

The dimensionless variables were chosen to facilitate the numerical solution of the modeling equations and expose time constants for key physicochemical processes involved. S, ζ, λ, X are dimensionless surface area, pore radius, pressure and gas concentration, respectively. ε^{ED}_{ij} and ε^{EP}_{ij} are dimensionless local effective diffusion and permeability coefficients, respectively. By defining $\eta = r^*/r_{oc}$ and $\xi = r/r^*$, where r^* is the instantaneous particle radius, the moving boundary problem is transformed to a fixed one. The second term on the right hand side of Equation 11 accounts for the effect of the moving boundary arising from shrinking particle size. The external surface of the particle receeds by two major mechanisms: chemical reaction on the external surface and perimeter fragmentation, as described by Equations 13 and 14, respectively. τ^* is the dimensionless time at which ϕ in Equation 11 reaches the critical porosity of fragmentation ϕ^*. The complete specification of the modelling equations requires working expressions for $\phi^A(\phi,z)$ and $\varepsilon^E(z,\phi,f(r),L(r))$ developed in Reyes and Jensen (17).

GASIFICATION IN THE KINETIC REGIME

In the kinetic regime CO_2 is uniformly distributed throughout the particle so only the rate of carbon consumption, according to Equation 11, is required to describe the gasification behavior. Furthermore, since only a negligible particle shrinkage occurs due to chemical reaction on the external surface, the second term on the right hand side of Equation 11 can be neglected. Because of the uniform porosity increase throughout the particle, Equation 14 predicts an instantaneous disintegration of the particle when ϕ reaches ϕ^*. For $\phi > \phi^*$ it can be shown that (21):

$$\phi = \frac{\phi^*}{\phi^* + (1-\phi^*)\exp\left[-Kr_{oc}\left[\tau-\tau^*\right]\right]} \qquad 16)$$

where r_{oc} is the initial particle radius, and ϕ is now a pseudo-porosity whose complementary fraction $(1-\phi)$ represents the remaining fraction of the initial solid

material. If conversion is related to ϕ through the relation:

$$X_{cp} = \frac{\phi - \phi_o}{1 - \phi_o} \qquad 17)$$

then the gasification rate is evaluated as:

$$\frac{dX_{cp}}{d\tau} = \begin{cases} \{\sigma_o \lambda X_{CO_2}/(1-\phi_o)\}S & , \tau < \tau^* \qquad 18a) \\ \dfrac{Kr_{oc}\phi^*(1-\phi^*)\exp\{-Kr_{oc}[\tau-\tau^*]\}}{(1-\phi_o)[\phi^* + (1-\phi^*)\exp\{-Kr_{oc}[\tau-\tau^*]\}]^2} & , \tau \geq \tau^* \qquad 18b) \end{cases}$$

Therefore, by using Equations 11, 16, 17 and 18 the complete gasification behavior of a char particle can be simulated. Typical kinetic and physical parameters chosen for this purpose are summarized in Table 2. It is assumed that micro- and mesopores are primarily responsible for the surface area and that they account for 2/3 and 1/3 of the pore volume, respectively. By using the general model equations it was verified that the parameter values in Table 2 correspond to gasification under kinetically controlled conditions. Figure 2 summarizes gasification behavior for porous char particles with different initial accessible porosities. A coordination number of z=7 was chosen to simulate a complex random structure giving a critical porosity of fragmentation of approximately 5/6, similar to values observed by Dutta et al. (23) and Kerstein and Niksa (19). The solid lines describe the gasification before particle disintegration. As expected, the higher the initial porosity the lower the conversion at which particle disintegration takes place. Beyond this critical conversion, the gasification of fragments is described by the dashed lines, as evaluated by Equations 16, 17 and 18b. The shapes of the rate curves reflect competition between surface area enlargement due to pore growth at low conversion, and surface area decay due to pore coalescence at larger porosities. With increasing values of initial porosities the coalescence process becomes important at shorter times, causing the maximum rate to decrease and shift towards lower values of conversion. Further increases in porosity cause the maximum to disappear.

The existence of closed pores, a topological feature of the internal structure, also plays a role in the gasification. Their existence has been experimentally determined by several investigators (e.g. 20 ,25). This effect can be readily illustrated by analyzing the behavior of char particles with different pore space connectivities. As observed from Figure 3, for a $\phi_o^A = 0.20$, the more connected the the internal structure is the higher the conversion at which particle disintegration takes place. In addition, as the connectivity is increased, the maximum rates decrease in magnitude and shift toward higher values of conversion. These phenomena are readily explained by noting that the lower the connectivity of the pore space is, the greater the amount of closed pores that can be made accessible by chemical reactions of pore walls. This in turn causes the accessible surface area to increase but also makes the rate of pore coalescence dominant at low conversions.

GASIFICATION IN THE DIFFUSIONAL REGIME

To clearly focus on transport limitations caused by intraparticle phenomena, it will be assumed that there is no boundary layer resistance for mass transport to the external surface (i.e. $B_{mi} >> 1$). The existence of boundary layer resistance can readily be included in the numerical solution but the interpretation of the results become unnecessarily more complicated. The modelling equations 7-15 were solved numerically by using orthogonal collocation on finite elements (23).

Once the onset of perimeter fragmentation has been reached, the global conversion and gasification rate depend not only on the gasification behavior of the

shrinking particle but also on the gasification history of the released fragments. By integrating Equation 17 throughout the particle and dividing by the particle volume, the global particle conversion is evaluated as:

$$\hat{X}_{cp}(\tau) = 3 \int_0^1 X_{cp}(\xi,\tau)\xi^2 d\xi \qquad 19)$$

Since released fragments react in a kinetic regime (21), their conversions and gasification rates are obtained by Equations 16, 17 and 18b. The global conversion of the fragments released at time τ_i is evaluated as:

$$\hat{X}_{cf}(\tau,\tau_i) = \frac{1 - \phi_o\{1 + [(1-\phi^*)/\phi^*] \exp[-Kr_{oc}(\tau-\tau_i)]\}}{(1-\phi_o)\{1 + [(1-\phi^*)/\phi^*] \exp[-Kr_{oc}(\tau-\tau_i)]\}} \quad , \quad \tau > \tau_i > \tau^* \qquad 20)$$

By weighting contributions from the shrinking particle and released fragments, the overall conversion behavior may be evaluated as:

$$\hat{X}_{cg}(\tau) = \eta^3(\tau)\hat{X}_{cp}(\tau) - \int_{\tau^*}^{\tau} \hat{X}_{cf}(\tau,\tau') \frac{d\eta^3(\tau)}{d\tau'} d\tau' \qquad 21)$$

The corresponding overall gasification rate, $d\hat{X}_{cg}(\tau)/d\tau$, is obtained by taking the time derivative of $X_{cg}(\tau)$ in Equation 21.

In order to illustrate the model predictions, the gasification behavior of a char particle at 1000°C with $\phi_o^A = 0.20$ and simulated with z=7 is presented. Other conditions as those in Table 2. Figure 4 shows CO_2 concentration profiles for different levels of carbon conversion. It is observed that as conversion increases, the profiles flatten out and approach the bulk concentration. This increase in concentration with burnoff is primarily caused by improved transport characteristics of the internal pore structure, as pore space is widened and made accessible. Since conversion increases most rapidly near the external surface, where the CO_2 concentration is high, the initial porosity for fragmentation is first reached at the particle surface when $\hat{X}_{cg} = 0.65$. While negligible particle shrinkage occurs because of chemical reaction on the particle surface, a rapid decrease in particle radius takes place by perimeter fragmentation.

The evolution of the dimensionless accessible surface area with carbon conversion is shown in Figure 5. In the early stages of conversion the surface area gradually grows due to pore enlargment as well as the contributions from closed pores. However, with increasing conversion, pore overlap between growing neighboring surfaces dominates over pore enlargement, causing the surface area to decrease. Because of the radially nonuniform conditions within the particle, the same qualitative surface area behavior occurs at each radial position but at different times. Even though this figure illustrates typical behavior during char gasification, it was previously shown that the surface area will not exhibit a maximum under conditions where pore overlap is already dominant from the beginning of the gasification.

The overall gasification curve for the above example is shown in Figure 6. This curve represents the often observed behavior where the rate goes through a maximum at some intermediate conversion. As intuitively expected, the conversion for maximum rate shifts toward higher values when the temperature is increased from a kinetic to a diffusional regime. Further temperature increase causes the critical conversion to decrease again, and eventually the maximum disappears, since in the limit of high temperature the particle reacts with a purely shrinking core behavior (SC). At $\hat{X}_{cg} = 0.65$ the onset of perimeter fragmentation is observed. At this point the rate exhibits an increase in its slope, which indicates an acceleration in the gasification process due to fragmentation phenomena. This acceleration effect is small in the present example because the high surface area of the particle segregates the solid structure into very small fragments (21), whose concentration before their

release is not much different from the bulk concentration. In this case, the acceleration is primarily due to the higher rates in the shrinking particle because of increasing overall transport rates with decreasing particle size. A much stronger effect would have been observed if external mass transport resistances were significant (i.e. $B_{mi} << 1$).

Figure 7 illustrates the change in particle size with particle conversion for different temperatures. At low temperatures the particle gasifies in the kinetic regime and disintegrates spontaneously when the critical porosity is reached. As diffusion resistance increases in importance with higher temperatures, perimeter fragementation occurs at lower conversions. In the limit of very high temperatures (i.e. reaction rates) perimeter fragmentation takes place from the beginning and the particle then follows the classical shrinking core (SC) behavior.

CONCLUSION

The application of percolation theory concepts to modelling of a single particle char gasification has been summarized. Emphasis has been placed on the interpretation and evaluation of transport and fragmentation properties of the changing pore structure during gasification. The qualitative behavior of the model in both the kinetically and the diffusionally controlled regimes clearly reflect the strong influence of structural properties on gasification. Furthermore, the good agreement between these model predictions and reported experimental observations (11,20,24-33) are encouraging for further use of percolation theory in modelling changing coal structures.

REFERENCES

1. Petersen, E. E., AIChE J. 3, 443-448 (1957).
2. Szekely, J. and J.W. Evans, Chem. Engng. Sci. 25, 1091-1097 (1970).
3. Hashimoto, K. and P.L. Silveston, AIChE J. 19, 259-268 (1973).
4. Simons, G.A. and M.L. Finson, Combust. Sci. Technol. 19, 217-225 (1979).
5. Simons, G.A., Combust. Sci. Technol. 19, 227-235 (1979).
6. Bhatia, S.K. and Perlmutter, D.D., AIChE J. 26, 379-386 (1980).
7. Bhatia, S.K. and Perlmutter, D.D., AIChE J. 27, 247-254 (1980).
8. Gavalas, G.R., AIChE J. 26, 577-585 (1980).
9. Gavalas, G.R., Combust. Sci. Technol. 24, 197-210 (1981).
10. Zygourakis, K., L. Arri and N.R. Amundson, Ind. Eng. Chem. Fundam. 21, 1-12 (1982).
11. Tseng, H.P. and T.F. Edgar, AIChE Annual Meeting, Los Angeles, CA (1982).
12. Reyes, S. and K.F. Jensen, Ind. Eng. Chem. Fundam. 23, 223-229 (1984).
13. Broadbent, S.R. and J.M. Hammersley, Proc. Camb. Phil. Soc. E3, 629-641 (1957).
14. Frisch, H.L. and J.M. Hammersley, J. SIAM, 11, 894-918 (1963).
15. Shante, V.K.S. and S. Kirkpatrick, Adv. Phys. 20, 325-357 (1971).
16. Hughes, B.D. and S. Prager, "The Mathematics and Physics of Disordered Media," Springer-Verlag, New York, 1-108 (1983).
17. Reyes, S. and K.F. Jensen, Annual AIChE Meeting, San Francisco, CA, Paper 35a (1984).
18. Fisher, M.E. and J.W. Essam, J. Math. Phys. 2, 609-619 (1961).
19. Kerstein, A.R. and S. Niksa, Int. Conference on Coal Science, Pittsburgh, PA, 743-746 (1983).
20. Turkdogan, E.T., R.G. Olson and J.V. Vinters, Carbon 8, 545-564 (1970).
21. Reyes, S. and K.F. Jensen, submitted to Chem. Engng. Sci.
22. Reyes, S. and K.F. Jensen, submitted to Chem. Engng. Sci.
23. Carey, G.F. and B.A. Finlayson, Chem. Engng. Sci. 30, 587-596 (1975).
24. Dutta, S., C.Y. Wen and R. J. Belt, Ind. Eng. Chem. Process Des. Dev. 16, 20-30 (1977).
25. Kawahata, M. and P.L. Walker, Jr., Proceedings 5th Carbon Conference, Pergamon Press, London, 251-263 (1962).

26. Walker, P.L. Jr., R.J. Foresti, Jr. and C.C. Wright, Ind. Eng. Chem. 45, 1703-1710 (1953).
27. Petersen, E.E., P.L. Walker, Jr. and C.C. Wright, Ind. Eng. Chem. 47, 1629-1630 (1955).
28. Walker, P.L. Jr. and E. Raats, J. Phys. Chem. 60, 364-369 (1956).
29. Berger, J., T. Siemieniewska and K. Tomkow, Fuel 55, 9-15 (1976).
30. Tomkow, K., A. Jankowska, F. Czechowski and T. Siemieniewska, Fuel 56, 101-106 (1977).
31. Dutta, S. and C.Y. Wen, Ind. Eng. Chem. Process Des. Dev. 16, 31-37 (1977).
32. Hashimoto, K., K. Miura, F. Yoshikawa and I. Imai, Ind. Eng. Chem. Process Des. Dev. 18, 72-80 (1979).
33. Foster, M. and K.F. Jensen, Int. Conference on Coal Science, Pittsburgh, PA, 464-467 (1983).

ACKNOWLEDGEMENT

This work was supported by DOE (DE/FG22-82PC50806) and the Graduate School of the University of Minnesota.

Temperature	Pressure	$D^E_{CO-CO_2}$ (a)	$D^E_{CO-CO_2}$ (b)
°C	atm.	cm^2/s	cm^2/s
18	1.0	0.0018	0.0014
500	1.0	0.0060	0.0069
600	1.0	0.0072	0.0083
700	0.1	0.043	0.041
700	0.2	0.035	0.032
700	0.5	0.018	0.019
700	1.0	0.0099	0.011
700	10.0	0.0012	0.0014
800	1.0	0.012	0.011
900	1.0	0.014	0.013

Table 1. Experimental and predicted effective diffusion coefficients in porous electrode graphite. (a) Experimental value, Turkdogan et al. (20), (b) Bethe network predictions (z=5).

Preexponential factor	:	$k = 5.0 \times 10^3$ (m/s)
Activation energy	:	$E_a = 60.0$ (kcal/mol)
Specific surface area	:	$S_o = 300.0$ (m^2/gr)
Particle radius	:	$r_{oc} = 200$ (μm)
Carbon density	:	$\rho_p = 1500$ (kg/m^3)
Rayleigh distribution		
smallest micropore radius	:	$r_{\mu o} = 10$Å
average micropore radius	:	$r_{\mu a} = 20$Å
smallest mesopore radius	:	$r_{Mo} = 50$Å
average mesopore radius	:	$r_{Ma} = 200$Å

Table 2. Kinetic and structural parameters used in the present simulations.

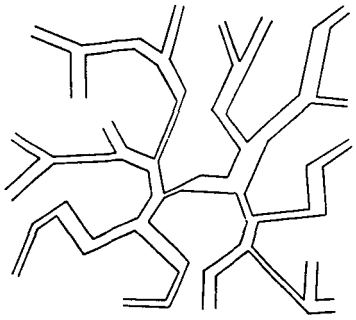

Figure 1. A schematic simulation of accessible porespace with a 3-coordinated Bethe network for arbitrary data of porosity and pore size distribution.

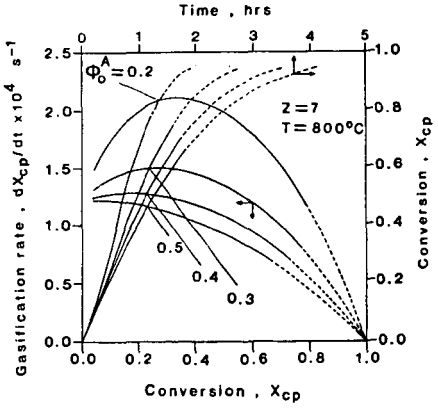

Figure 2. Conversion vs. time and gasification rate vs. conversion for a char particle for various initial porosities.

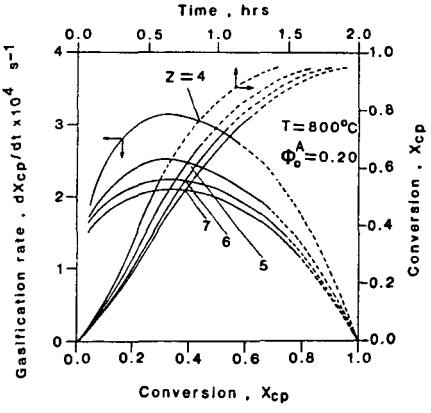

Figure 3. Conversion vs. time and gasification rate vs. conversion for a char particle with different porespace connectivities.

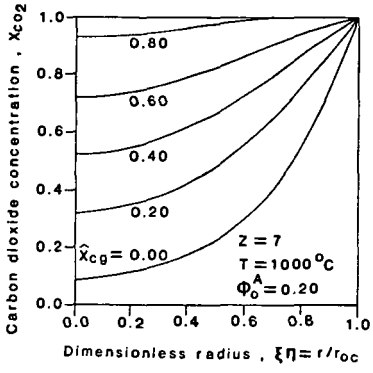

Figure 4. Carbon dioxide concentration profiles at various levels of overall conversion.

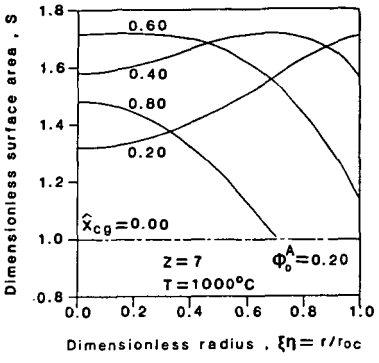

Figure 5. Dimensionless surface area profiles at various levels of overall conversion.

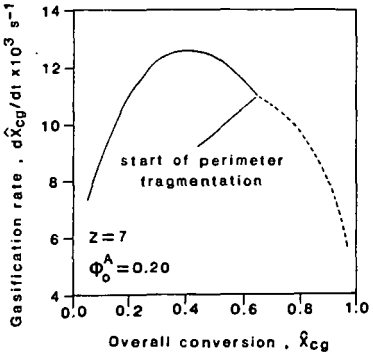

Figure 6. Gasification rate vs. conversion for a char particle at 1000°C.

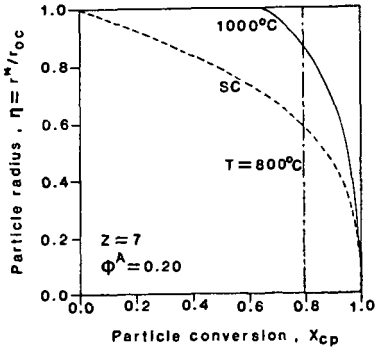

Figure 7. Particle radius as a function of particle conversion for a char particle for various reaction temperatures.